

The Role of Long-Alkyl-Group Spacers in Glycolated Copolymers for High-Performance Organic Electrochemical Transistors

Ellasia Tan, Jingwan Kim, Katherine Stewart, Charalampos Pitsalidis, Sooncheol Kwon, Nicholas Siemons, Jehan Kim, Yifei Jiang, Jarvist M. Frost, Drew Pearce, James E. Tyrrell, Jenny Nelson, Roisin M. Owens, Yun-Hi Kim,* and Ji-Seon Kim*

Semiconducting polymers with oligoethylene glycol (OEG) sidechains have attracted strong research interest for organic electrochemical transistor (OECT) applications. However, key molecular design rules for high-performance OECTs via efficient mixed electronic/ionic charge transport are still unclear. In this work, new glycolated copolymers (gDPP-TTT and gDPP-TTVTT) with diketopyrrolopyrrole (DPP) acceptor and thiophene (T) and vinylene (V) thiophene-based donor units are synthesized and characterized for accumulation mode OECTs, where a long-alkyl-group (C_{12}) attached to the DPP unit acts as a spacer distancing the OEG groups from the polymer backbone. gDPP-TTVTT shows the highest OECT transconductance (61.9 S cm^{-1}) and high operational stability, compared to gDPP-TTT and their alkylated counterparts. Surprisingly, gDPP-TTVTT also shows high electronic charge mobility in a field-effect transistor, suggesting efficient ion injection/diffusion without hindering its efficient electronic charge transport. The elongated donor unit (TTVTT) facilitates hole polaron formation to be more localized to the donor unit, leading to faster and easier polaron formation with less impact on polymer structure during OECT operation, as opposed to the TTT unit. This is supported by molecular dynamics simulation. These simultaneously high electronic and ionic charge-transport properties are achieved due to the long-alkyl-group spacer in amphipathic sidechains, providing an important molecular design rule for glycolated copolymers.

1. Introduction

Organic electrochemical transistors (OECTs) have drawn great interest for their technological applications in energy storage, biosensing and biomedical diagnostics.^[1–7] The OECTs utilize a three terminal device architecture similar to organic field effect transistors (OFETs). However, differently from the solid-state OFETs, OECTs operate with an electrolyte between the gate and the channel of the transistor, rather than a dielectric film. A voltage applied at the gate electrode then enables the ion injection in the channel and subsequently modulates the charge-carrier density via electrochemical doping/dedoping of the polymer.^[8–10] The OECT device performance is measured by a peak transconductance ($g_m = \partial I_D / \partial V_G$)—the ability to transduce a gate voltage (V_G) modulation to drain current (I_D) modulation.^[11] Due to the mixed conduction induced by electronic and ionic charges in OECTs, it is important to synthesize organic materials that optimize both electronic and ionic conduction.

E. Tan, K. Stewart, N. Siemons, J. M. Frost, J. Nelson, J.-S. Kim
Department of Physics and the Centre for Processable Electronics
Imperial College London
Prince Consort Road, London SW7 2AZ, UK
E-mail: ji-seon.kim@imperial.ac.uk

J. Kim, Y. Jiang, Y.-H. Kim
Department of Chemistry and Research Institute of Green Energy
Convergence Technology (RIGET)
Gyeongsang National University
Jinju, Gyeongnam 660–701, South Korea
E-mail: ykim@gnu.ac.kr

 The ORCID identification number(s) for the author(s) of this article can be found under <https://doi.org/10.1002/adma.202202574>.

© 2022 The Authors. Advanced Materials published by Wiley-VCH GmbH. This is an open access article under the terms of the Creative Commons Attribution License, which permits use, distribution and reproduction in any medium, provided the original work is properly cited.

DOI: 10.1002/adma.202202574

C. Pitsalidis
Department of Physics, Healthcare Engineering Innovation Center (HEIC)
Khalifa University
Abu Dhabi P. O. Box 127788, UAE

C. Pitsalidis, R. M. Owens
Department of Chemical Engineering and Biotechnology
University of Cambridge
Philippa Fawcett Drive, Cambridge CB3 0AS, UK

S. Kwon
Department of Energy and Materials Engineering
Dongguk University-Seoul
Seoul 04620, Republic of Korea

J. Kim
Pohang Accelerator Laboratory
Pohang University of Science and Technology
Pohang 37673, Republic of Korea

D. Pearce, J. E. Tyrrell
Experimental Solid State Physics Group, Department of Physics
Imperial College London
Prince Consort Road, London SW7 2AZ, UK

A conducting polymer, poly(3,4-ethylenedioxythiophene):poly(styrenesulfonate) (PEDOT:PSS), has been the champion organic material for OECT biological applications with high transconductances reaching as high as 10^3 S cm^{-1} using various processing methods.^[12–14] In the case of PEDOT:PSS-based devices which operate in the depletion mode, a positive gate bias lowers the conductance or switches off the device via an electrochemical de-doping process. This leads to undesirable high-power consumption even in the OFF state and reduces their practicality for biological applications that require less power usage. The depletion mode operation can also limit biosensing applications, due to them being particularly sensitive to delamination or degradation and its subsequent interference on the sensing current.^[3] As such, it is more desirable for the device to switch ON upon a biological event. Consequently, there is a clear necessity to synthesize organic OECT materials which can operate in accumulation mode, that is, low current in their neutral state (OFF at $V_G = 0$) and high current when electrochemically doped (ON at $V_G < 0$). Such accumulation mode OECT devices can be readily achieved by using semiconducting conjugated polymers due to their lower intrinsic charge-carrier density and conductivity. By synthetically tailoring the molecular structures of the conjugated backbone or sidechains, their charge-conduction pathways and electrochemical stability can be optimized.^[3,15–17]

One design strategy for accumulation mode OECT conjugated materials is to functionalize polymers with polar sidechains such as oligoethylene glycol (OEG) to increase ion uptake into the bulk polymer film.^[18,19] This leads to more ion-accessible sites within the channel, allowing more ions to electrochemically dope the polymer. With an increased availability of counterions close to the polymer backbone, more electronic charge carriers are generated. As such, the volumetric capacitance (C^*) is greatly enhanced, which contributes to high OECT transconductance.^[15,19] However, the increased structural disorder of the conjugated polymers often induced by the glycol sidechains impedes electronic charge transport by lowering carrier mobilities (μ).^[20] Therefore, there should be a fine balance in optimizing the transconductance which is the product of the two important parameters, that is μC^* , in OECT devices based on glycolated polymers. Instead of using full OEG sidechains, a short ethyl group spacer in amphipathic sidechains can be used to increase polymer crystallinity and OECT transconductance.^[21] Other studies with spacers ranging from C_3 to C_6 groups in n-type and thiophene homopolymers have shown that excessive swelling can be reduced to improve electronic charge transport.^[22,23] The alkyl-group spacers have also shown promise in thermoelectric applications, where the Seebeck coefficient is increased without diminishing energetic order.^[24] Another strategy is tuning the conjugated backbone structure of polymers from homopolymers such as poly(3-hexylthiophene) (P3HT) to donor–acceptor (D–A) type copolymers.^[3,15,16,25] Some advantages of using D–A type copolymers include tuneable coplanarity, energetics and intrachain/interchain properties, which then affects device properties.^[26–28] For example, by controlling the electron-rich nature of the donor unit and adding a methoxy group onto thienothiophene, alkoxy benzodithiophene copolymers showed better device stability.^[27] High OECT performance was also achieved by greater molecular

order and delocalization of charge density in DPP copolymers by changing donor moieties.^[28] These studies have shown great potential to improve OECT performance and stability by tuning the polymer molecular structures, particularly showing promise of alkyl-group spacers in amphipathic sidechains.

In this work, we focus on the long-alkyl-group spacer in glycolated copolymers and its impact on D–A OECT materials, which has not been addressed previously. We synthesize and characterize new glycolated diketopyrrolopyrrole (DPP)-based copolymers containing thiophene (T) or vinylene (V) with thiophene as a donor unit (TTT or TTVTT). Differently from other work, our molecular design features a long C_{12} alkyl spacer on the polar sidechains, further distancing the OEG groups away from the main conjugated backbone, defined as amphipathic sidechains. The sidechains of the new copolymers are modified to have branched long alkyl chains (DPP-TTVTT and DPP-TTT) or amphipathic sidechains (gDPP-TTVTT and gDPP-TTT). By using DPP-based D–A type copolymer structures, we take advantage of their initially strong optoelectronic and morphological properties that is beneficial for charge transport.^[29–32] The TTVTT unit is used to elongate the conjugated backbone of the copolymers, thus tuning the material properties.^[31–33] Based on an assay of spectroscopic and structural measurements including in situ electrochemical Raman spectroscopy and grazing-incidence wide-angle X-ray scattering (GIWAXS), we identify the effects of the elongated conjugated backbone and long-alkyl-group spacers on the solid-state packing and charge-transport properties. First, the amphipathic sidechains preserve well-ordered “edge-on” molecular packing of DPP-TTVTT but alter DPP-TTT’s packing from “face-on” to “edge-on”. As the “edge-on” packing is ideal for efficient lateral electronic charge transport, high OFET hole mobilities are achieved for the glycolated copolymers. Second, the strongly polar amphipathic sidechains allow efficient ionic injection/diffusion into the copolymers leading to significant increase in the OECT transconductances. Third, gDPP-TTVTT experiences less pronounced structural changes upon polaron formation, as the DPP acceptor vibrational modes are less affected. Thus, gDPP-TTVTT localizes polarons more across the TTVTT donor units than the DPP acceptor units. The elongated conjugated backbone (DPP-TTVTT) and amphipathic sidechains of gDPP-TTVTT facilitate efficient and increased polaron formation at lower voltages, leading to the high OECT device performance and operational stability. These findings demonstrate that the C_{12} spacer is extremely beneficial for improving OECT performance by providing efficient ion injection/diffusion without disturbing the lateral electronic charge transport of the copolymers.

2. Results and Discussion

2.1. Devices and Electrical Characterization

The four DPP copolymers are synthesized by Stille coupling reaction and the chemical structures are shown in **Figure 1a** for DPP-TTT, gDPP-TTT, DPP-TTVTT and gDPP-TTVTT. The full synthetic scheme and detailed synthesis of the new gDPP-Br monomer and copolymers are outlined in the Supporting Information. For each copolymer, the molecular design is defined by

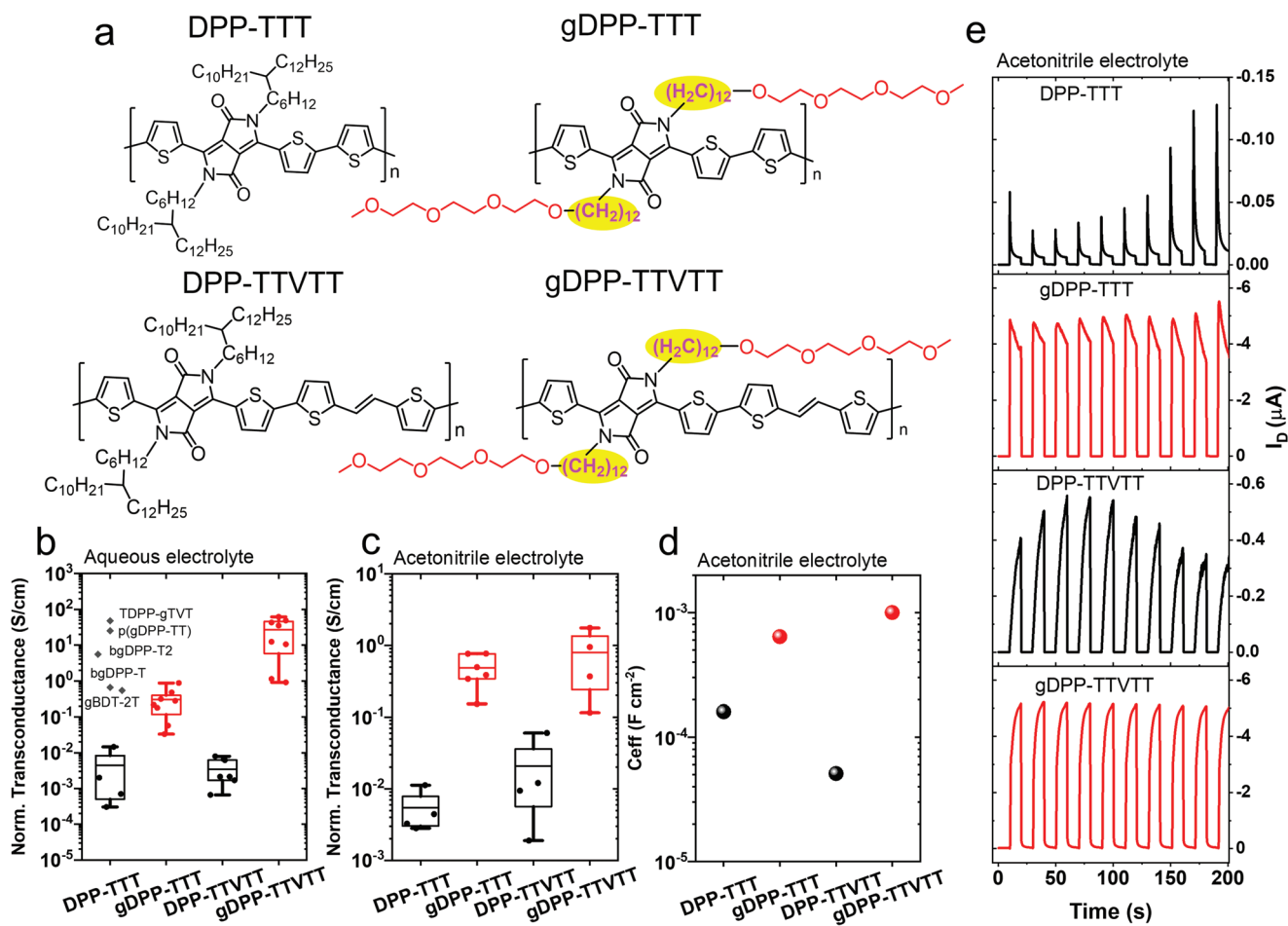


Figure 1. a) Chemical structures of the four DPP copolymers: DPP-TTT, gDPP-TTT, DPP-TTVTT, and gDPP-TTVTT. b, c) OECT transconductances taken from the derivative of the transfer characteristics, normalized by Wd/L (where W is width, L is length, and d is thickness of channel) and using 2 types of electrolytes: b) Ringer's solution (2mm/200 μm – W/L) and c) 0.1 M tetrabutylammonium hexafluorophosphate (TBAPF₆) acetonitrile electrolyte (100/10 μm – W/L). Each datapoint represents a device and the additional datapoints marked as gray diamonds in (b) are taken from the literature for comparison with other similar copolymers.^[26–28,34] The statistical box plot with individual device data points show the device-to-device variation including a mean line, box data range of 25–75% and whiskers of max and min values. d) The effective capacitance per unit area (C_{eff}) at 1Hz extracted using a modified Randles' cell equivalent circuit $R_s(Q_p||R_p)$ shown in the Supporting Information. e) Transient OECT measurement of I_D changes over 200 s while the V_C is pulsed between 0 and -0.8 V for OFF and ON regimes, respectively.

two distinct features: choice of conjugated backbone and choice of sidechains. Importantly, we incorporate a long-alkyl-group (C₁₂) between the conjugated backbone and the triethylene glycol end-groups. These amphipathic sidechains are intended to minimize any adverse effects on the conjugated backbone (i.e., electronic charge transport), while maximizing the benefits of increased polarity for electrochemically driven devices.

First, we integrate the copolymers as active channels in OECT devices to evaluate the effect of molecular structure engineering on device performance and stability. The transconductances are derived from the transfer characteristics (Figures S6,S7, Supporting Information) and normalized by channel dimensions (Wd/L). Note that the aqueous and acetonitrile electrolyte driven OECTs share the same W/L ratio despite the different device architectures as outlined in the Supporting Information. Nevertheless, both types of OECTs show the same trend of improvement in transconductance upon the exchange of branched alkyl to amphipathic sidechains with

long-alkyl-group spacers. The highest transconductance in acetonitrile electrolyte was recorded at 0.76 and 1.75 S cm⁻¹ and in aqueous electrolyte at 0.87 and 61.9 S cm⁻¹, for gDPP-TTT and gDPP-TTVTT respectively. As highlighted in Figure 1b, their performances are comparable to previously reported similar accumulation mode copolymers with full OEG sidechains (range from 1 to 25 S cm⁻¹).^[15,26–28,35] In particular, gDPP-TTT that shares the same backbone structure as b(gDPP-T2) with branched full OEG sidechains, shows the transconductance is within an order of magnitude.^[26] Whereas gDPP-TTVTT's transconductance reaches higher or the same order of magnitude (10² S cm⁻¹) to the state-of-the-art DPP copolymers with full OEG sidechains.^[27,28,34] This is especially impressive as this study's copolymers have a smaller fraction of polar component than others reported, consisting of a C₁₂ alkyl spacer with OEG end groups. Exchanging the alkyl to amphipathic sidechains also reduces the OECT threshold voltages (V_{Th}) (Figure S8 and Table S1, Supporting Information).^[4] The V_{Th} indicates

the voltage at which the OECT switches on.^[36,37] This is closely linked to the energetics as low voltage operation require shallower highest molecular orbital (HOMO) energy levels for efficient charge injection and facile electrochemical oxidation.^[4,38] The minimum V_{Th} (extracted from $I_D^{0.5}$ vs V_G plots) shifts from -0.47 to -0.40 V and -0.43 to -0.37 V going from DPP-TTT and DPP-TTVTT to gDPP-TTT and gDPP-TTVTT, respectively. Overall, the amphipathic sidechains improve transconductance by 2–4 orders of magnitude and lower V_{Th} , with gDPP-TTVTT achieving the highest OECT performance.

To quantify the capacitive and resistive behavior of the copolymers, the experimental electrochemical impedance spectroscopy (EIS) data (at $V_{offset} = 0.8$ V) were fitted using a modified Randles cell ($R_s(Q_p||R_p)$) equivalent circuit model (Figure S9, Supporting Information). Fit results are summarized in Table S2, Supporting Information and Figure 1d showing that gDPP-TTT and gDPP-TTVTT have effective capacitance values of 0.64 and 1.00 mF cm⁻², compared to DPP-TTT and DPP-TTVTT only reaching 0.16 and 0.05 mF cm⁻², respectively. The amphipathic sidechains increase the effective capacitance, which ultimately improves transconductance as a key factor. This is also observed qualitatively in the cyclic voltammetry (CV) scans (optoelectronic properties section), as there is an overall increase of current density during oxidation for the glycolated copolymers. The general trend of the effective capacitance and the electrochemical characteristics (CV and transconductance) are all in excellent agreement. Furthermore, the phase Bode spectra (Figure S10, Supporting Information) reveal an almost ideal capacitive behavior for the glycolated copolymers, with phase angle values ranging between 45° and 90° at the low frequency regime (<100 Hz), while the alkylated copolymers exhibit a more distinct capacitive behavior (phase peak of ≈70°) only at the high frequency regime (>1 kHz). As such, gDPP-TTT and gDPP-TTVTT exhibit a more efficient bulk ion injection compared to the alkylated copolymers. The inefficient ion injection of DPP-TTT and DPP-TTVTT can be attributed to the formation of a double layer capacitance at the electrode/electrolyte interface, which impedes the penetration of ions to the bulk of the polymer. Previous studies have controlled volumetric electrochemical doping with full OEG sidechains and varying percentage of glycol comonomers.^[20,35] However, we demonstrate that amphipathic sidechains with long-alkyl-group spacers (C₁₂) is also an effective method for increasing capacitance by a maximum of 20 fold, without the necessity for full OEG sidechains on the copolymers.

For synthesis of future OECT materials, it is equally important to understand the effects of molecular design on electrochemical stability as well as performance. The forward and backward voltage sweeps in output and transfer characteristics show minimal hysteresis for the glycolated copolymers (gDPP-TTT and gDPP-TTVTT). This is an indication of enhanced ionic diffusion inducing faster electronic charge generation and extraction.^[19,39] In contrast, there is significant hysteresis of the alkylated polymers, indicative of the less efficient ion diffusion. In Figure 1e, the transient V_G pulses between 0 and -0.8 V defining the ON and OFF regimes, shows the changes in I_D over time. Both gDPP-TTT and gDPP-TTVTT exhibit an increase in the maximum ON current (at the same V_G) after output and transfer sweeps. This is a common occurrence in

transistors and the result of filling charge-carrier traps during voltage sweeps.^[40,41] The initial electrical measurements will also cause swelling of the polymer film assisting more effective ion diffusion thus increasing polaron formation in the subsequent measurements. Focusing on the stability of the transient characteristics, the alkylated copolymers exhibit non-uniform I_D , showing large changes in ON current during repeated OECT operations of pulsed gating cycles. In contrast, glycolated copolymers have stabilized I_D over repeated OECT operations and significantly reduced degradation of ON current during operation. The transient characteristics of gDPP-TTT show a gradual loss in ON current (≈15%), while gDPP-TTVTT has no ON current degradation.

As the OECT is a mixed electronic and ionic conduction device, the electronic conduction will have a significant contribution to the OECT performance. To differentiate the effect of the molecular design on the two separate conduction pathways, we investigate the materials in solid-state OFET devices and study the electronic (hole) charge-transport properties separately. Specifically, the OFET hole mobility is the figure-of-merit used to evaluate the efficiency of the electronic charge transport in the polymers.^[42]

In **Figure 2**, there is a marked difference between the two alkylated copolymers. DPP-TTT shows a comparably inferior performance with a saturated mobility of 0.05 cm² V⁻¹ s⁻¹ with high hysteresis and shallow sub threshold slope. In contrast, DPP-TTVTT measures a higher mobility (0.09 cm² V⁻¹ s⁻¹) and the shape and hysteresis of the transfer curve indicate a much faster switching speed with fewer traps. The same DPP-TTVTT copolymer was also previously tested by Kim et. al. in OFETs and the maximum hole mobility was reported at 10.54 cm² V⁻¹ s⁻¹.^[33] The lower mobilities in this study are caused by the unoptimized pre-fabricated OFET substrates. Despite this, we still observe clear disparity in hole mobility of DPP-TTT and DPP-TTVTT suggesting that there is a significant difference in electronic charge-transport behavior caused by the elongated conjugated polymer backbone.

Comparing the transfer curve between alkylated and glycolated OFETs shows how electronic charge transport is affected as the sidechains are modified. Going from DPP-TTT to gDPP-TTT, the saturated hole mobility increases (0.05–0.06 cm² V⁻¹ s⁻¹). The hysteresis in the transfer curves is minimized with the glycolation for DPP-TTT copolymers. This suggests an improved efficiency of charge injection and extraction, like the enhanced ion-dependent electronic charge transport seen in the OECTs. In contrast, the glycolation does not significantly affect DPP-TTVTT as the hole mobility is maintained (0.09 cm² V⁻¹ s⁻¹) and hysteresis remains low. High charge-carrier mobilities will also contribute as a key factor towards the transconductance in OECTs. Hence, gDPP-TTVTT achieves the highest upper limit of transconductance as it is capable of more efficient hole charge transport. The mobility trends clearly show that positioning the OEG groups away from the conjugated backbone ensures that the electronic charge transport is undisturbed.

GIWAXS is used to determine the solid-state packing structure and establish correlations between the OFET device performance and morphology. **Figure 3a** presents the 2D GIWAXS patterns of the DPP-TTT, gDPP-TTT, DPP-TTVTT, and gDPP-TTVTT thin film, respectively. The corresponding one-dimensional

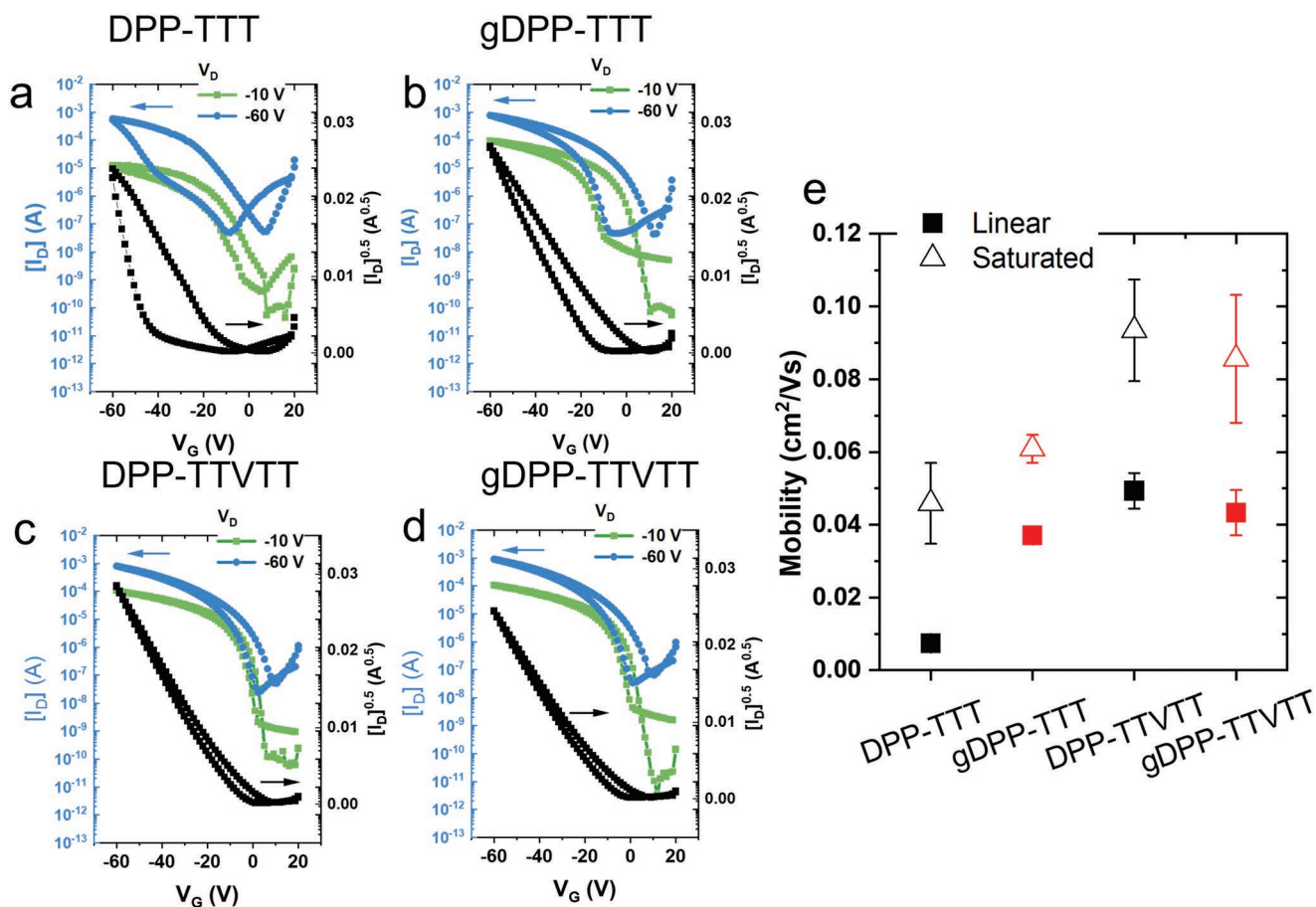


Figure 2. a–d) OFET transfer plots (I_D – V_G and $I_D^{0.5}$ – V_G) for a set of 5 μm channel length, sweeping V_G from 20 to -60 V and constant drain voltage (V_D) = -10 and -60 V. e) OFET linear and saturated hole mobility values extracted using an average of transfer characteristics. The error bars indicate the standard deviation extracted from a collection of 4 device channels per copolymer.

scattering profiles from the 2D GIWAXS patterns along the in-plane ($q_{x,y}$) and out-of-plane (q_z) directions are shown in Figure 3b and tabulated in Table S4, Supporting Information. For DPP-TTT, several diffraction peaks are observed along the in-plane and out-of-plane direction ($q_{x,y}$ (\AA^{-1}) = 0.21, 0.38, 0.57 and q_z (\AA^{-1}) = 0.26, 0.41, 0.58), which are related to lamellar spacing of the (100), (200) and (300) plane. However, there is only 1 scattering peak associated with the π stacking distance of the (010) plane along the out-of-plane direction at q_z (\AA^{-1}) = 1.70 ($2\pi/1.70 = 3.70$ \AA). This indicates that DPP-TTT possesses a bimodal molecular packing with a “face-on” dominant orientation. After glycolation (gDPP-TTT), the lamellar spacing for the (100), (200), and (300) plane along the q_z axis appear more intense while the peaks along the $q_{x,y}$ disappears. The strong π stacking of the (010) plane at $q_{x,y}$ (\AA^{-1}) = 1.67 ($d = 3.77$ \AA) is also developed, showing an evolution towards the “edge-on” orientation in the DPP-TTT film due to the amphipathic sidechains (illustrated in Figure 3c). “Edge-on” orientation is beneficial for lateral charge transport as the π – π stacking is now parallel to the substrate. This correlates well with the OFET characteristics and explains the drastic improvement of hole mobility, after the glycolation of DPP-TTT. Such a change in molecular orientation is likely to result from the reduced steric hindrance and side-chain density in gDPP-TTT relative to DPP-TTT by changing

branched to linear sidechains.^[15,43] This also results in shorter lamellar stacking distances for gDPP-TTT (and gDPP-TTVTT, as shown below) (Table S4, Supporting Information), due to better interdigitation of the long-alkyl-group spacers in the amphipathic sidechains compared to branched alkyl sidechains.

In contrast to DPP-TTT, the greater intensity of DPP-TTVTT diffraction peaks highlight greater order of out-of-plane lamellar packing and in-plane π stacking orientation, resulting in “edge-on” packing structure. The elongated conjugated backbone reduces sidechain density, thus lowering lamellar stacking distance from 29.7 to 24.8 \AA . Compared to DPP-TTVTT, gDPP-TTVTT has slightly reduced intensity of diffraction peaks but maintains its “edge-on” character. This is indicative of fewer molecules orientated at edge-on upon glycolation. The π stacking distance of gDPP-TTVTT also increases (3.67–3.72 \AA) and indeed, gDPP-TTVTT has slightly lower hole mobility than DPP-TTVTT. However, as the relatively high “edge-on” molecular order is well-preserved, there are only minor changes of OFET mobilities for gDPP-TTVTT. Despite the small increase in π stacking distances in gDPP-TTT and gDPP-TTVTT, they remain comparable to other OEG-modified polymers in the literature (3.54–4.40 \AA).^[15,20,44,45] The slight increase in π stacking distance and molecular packing disorder can enhance ion diffusion pathways

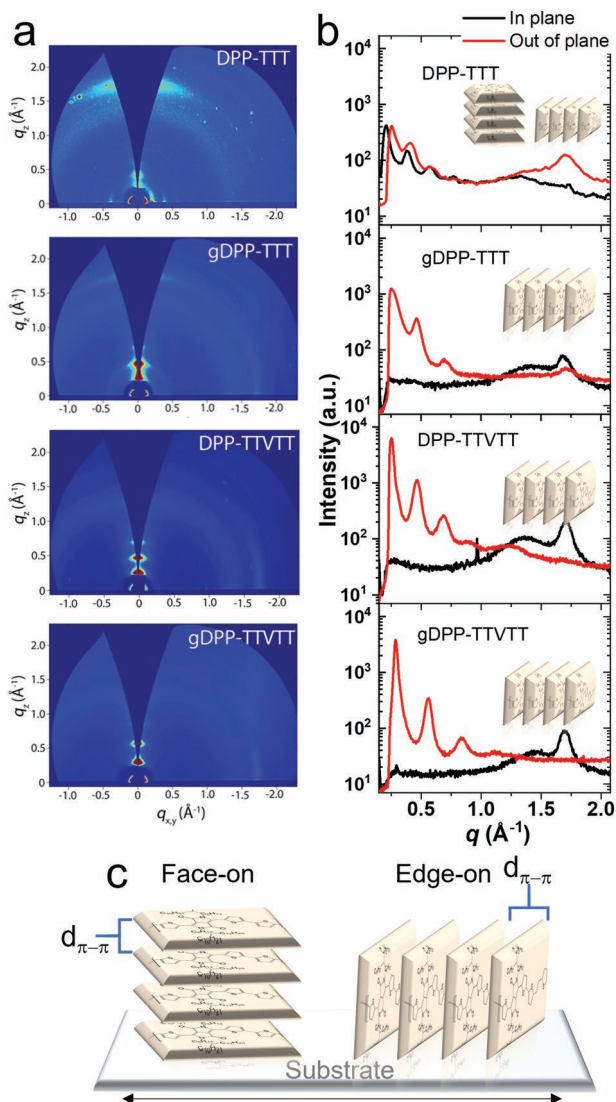


Figure 3. a) 2D GIWAXS patterns for the four copolymers and b) GIWAXS diffractograms for in-plane and out-of-plane scattering with illustrative insets of the dominant molecular orientation that the copolymer adopts in thin films. DPP-TTT has a “face-on” dominant bimodal orientation whereas all other copolymers adopt “edge-on” orientation. c) Illustration of the structural packing orientations including “face-on” and “edge-on” relative to the substrate.

upon hydration in OECTs, as polymer expansion occurs easier with fewer crystalline regions.^[25,26] The use of OEG sidechains typically improves solubility and lowers polymer aggregation in polar processing solvents, which can induce “face-on” molecular orientation.^[20,45] However, the amphipathic sidechains with long-alkyl-group spacers preferentially induces the “edge-on” molecular orientation, proving beneficial for hole transport. Additionally, these D–A copolymers with amphipathic sidechains continue to exhibit high molecular order with three clear orders of lamellar stacking peaks in the out-of-plane direction. This indicates a significant number of highly ordered “edge-on” crystallites particularly in comparison to similar DPP copolymers with full OEG sidechains which show a lower order of solid-state packing.^[26,28] As such, pre-

vious studies with full OEG sidechains typically resulted in an inverse relationship between transconductance or capacitance and mobility.^[20,45] Our molecular design using the long-alkyl-group spacer in amphipathic sidechains overcomes this trade-off between ionic and electronic charge transport. Therefore, the glycolated copolymers benefit from high transconductance, while adverse effects on the conjugated backbone and electronic charge transport are minimized.

2.2. Optoelectronic Properties

We further investigate the change in optical and electronic properties of the copolymers upon changing the backbone and sidechain, as they are critical to determining charge-transport properties. Figure S11a, Supporting Information presents the UV–vis–NIR absorption spectra of the polymer thin films. All copolymers show a weak π – π^* transition band around 350–500 nm and a strong intramolecular charge-transfer band around 550–1000 nm.^[31,46] By elongating the conjugated backbone and observe narrowing of the full-width half maximum (FWHM) by 28 nm, going from DPP-TTT to DPP-TTVTT. This is also reflected in the π – π^* transition higher energy band being red-shifted by 34 nm for the DPP-TTVTT copolymers, typically associated with higher molecular order and longer effective conjugation lengths.^[47] The emergence of the vibronic shoulder at 700 nm, on the lower energy band for the DPP-TTVTT copolymers, also supports the rise in crystalline aggregate regions.^[31,32] On the other hand, exchanging the alkyl to amphipathic sidechains causes broadening of the absorption spectrum with larger FWHM, highlighting the increase in energetic disorder.^[20]

The HOMO energy levels of the four copolymers (Figure S11b,c, Supporting Information) are established using CV. DPP-TTT HOMO energy level is deep, lying at -5.63 eV, compared to DPP-TTVTT at -5.44 eV. This is also seen in DFT simulations of the isolated molecules (Figure S12, Supporting Information). The amphipathic sidechains also influences the energetics, shallowing HOMO energy levels (given by CV) by 0.49 and 0.31 eV for gDPP-TTT and gDPP-TTVTT, respectively. The HOMO energy level extracted from the thin film CV scans of the copolymers is directly associated with the ease of electrochemical oxidation of polymer film.^[15,19] Due to the increased polar components of the amphipathic sidechains in gDPP-TTT and gDPP-TTVTT, there is more efficient bulk ion injection, as observed in the EIS. This results in the glycolated copolymers being easier to oxidize at lower voltages, thus shallowing HOMO energy levels, which is advantageous for low-voltage operation in the OECT. The magnitude of change in energetics resulting from the amphipathic sidechains is greater than those reported previously using full OEG sidechains.^[19] Note that due to an initially deeper HOMO energy level, the glycolation has a greater impact on the shift of the DPP-TTT copolymer than that of DPP-TTVTT. Despite the difference in magnitude of the shift, the HOMO levels of the glycolated polymers are at similar energies around -5.14 eV, highlighting the dominant impact of the amphipathic sidechains on the energetics.

2.3. In Situ Structural Analysis upon Electrolyte Immersion and Polaron Formation

We use in situ Raman and UV–vis spectroscopy with an electrochemical cell to probe the neutral polymer upon electronic charge (hole) injection and polaron formation induced by ions during electrochemical doping.^[4,48] Differently from previous studies, we elucidate the exact nature of electrochemical interactions between the conjugated polymers and ions, and their impact on OECT performance and stability. As polaron formation is accompanied by lattice reorganization, the in situ structural techniques are extremely relevant to understand the structure-function relationships for OECT materials. For greater sensitivity to the conjugated backbone in Raman spectroscopy (Figure 4), 488 nm excitation wavelength is selected to be resonant with the π – π^* electronic transition delocalized along the conjugated backbone.^[46,48–51] This was determined via UV–vis spectral changes upon applied oxidizing potentials (Figure S13a, Supporting Information). As the oxidizing potential is gradually increased, the ground state absorption quenches due to the transformation of neutral to oxidized species. The trend in absorbance values extracted from the maximum intensity of the lower energy band (at 785 nm) are shown in Figure S13b, Supporting Information. This confirms the reduction of the oxidation onset after glycolation, as the ground state absorbance is quenched at less positive voltages for gDPP-TTT and gDPP-TTVTT. Going from DPP-TTT to gDPP-TTT, compared to DPP-TTVTT to gDPP-TTVTT, the onset for the quenching of the ground state is lowered by 0.3 and 0.2 V, respectively. Like the energetics, there is a larger effect of amphipathic sidechains for DPP-TTT. However, gDPP-TTVTT shows more quenching of the ground state at the same applied potentials suggesting greater polaron formation.

We further analyze the changes in the main vibrational modes upon electrochemical doping and relate the polaron formation in the electrochemical cell to the OECTs. The vibrational mode assignments were made according to the DFT simulations (Figure S14, Supporting Information) and literature.^[32,46] Peaks 1 and 2 are associated with the donor (thiophene) C–C_{intra} and C–C_{inter}, while peak three has major contributions from the acceptor (DPP) C–N and C–C_{intra} (Figure 4a). Prior to applying an oxidative bias, a normalized comparison of the solid-state and electrolyte immersed thin films is shown in Figure 4b. All four copolymers exhibit some amount of structural and π -electron density changes upon immersion in electrolyte (intensity changes shown in Figure S15, Supporting Information). gDPP-TTVTT is the least structurally changed, whereas gDPP-TTT is strongly affected by the electrolyte like the alkylated copolymers. Although all copolymers have selective quenching of certain Raman peaks upon immersion, only gDPP-TTT selectively quenches peak 3. This indicates a shift in π -electron density from the acceptor to donor units upon electrolyte immersion.

Figure 4c investigates the structural changes upon electrochemical doping. Spectral quenching of vibrational modes occurs as the film is biased, sweeping from 0 to 0.9 V versus Ag oxidizing potentials. Under resonant Raman conditions, the intensity of the peaks largely depends on the number of neutral species that has a ground state π – π^* electronic transition

around 488 nm.^[49,50,52] Hence, the intensity quenching is explained by the transformation of neutral to polaron species, which is no longer in resonance with the excitation wavelength. To quantify the degree of spectral quenching, the changes in Raman intensity for peaks 1–3 are extracted and shown in Figure 4d. For all copolymers, spectral quenching occurs for peaks 1–2 thereby, forming polarons with structural changes in the donor units' C–C_{intra} and C–C_{inter} bonds. However, there are differences in the degree of structural changes at each oxidizing potential. Between the alkylated copolymers, the spectral quenching of donor units (peak 1 and 2) in DPP-TTVTT is greater and occurs at lower oxidizing potentials than DPP-TTT. This correlates well with DPP-TTVTT's shallower HOMO energy level and increased ground state quenching in the spectroelectrochemistry. This effect is enhanced upon glycolation with greater bleaching of peaks 1 and 2, at lower oxidizing potentials. gDPP-TTVTT especially shows larger spectral changes at lower voltages, suggesting that the polaron formation is faster and greater at lower oxidizing potentials. This agrees with gDPP-TTVTT's higher effective capacitance, OECT transconductance and lower V_{Th} .

In contrast to donor units' peaks 1–2, the vibrational mode (peak 3) assigned to only the DPP acceptor units' C–N and C–C_{intra}, is maintained at a high Raman intensity throughout the oxidation for most copolymers. Such selective quenching of peaks 1–2 without peak 3, means that the DPP acceptor unit is less structurally changed and involved in the electrochemical doping process. Therefore, upon polaron (hole) formation, there is non-uniform charge distribution in these D–A copolymers with more usage of the donor units. Exchanging alkyl to amphipathic sidechains for gDPP-TTVTT maintained this selective quenching of peaks 1–2 without peak 3 thus, primarily using the donor groups for polaron formation. However, for gDPP-TTT, there is spectral quenching of all peaks including peak 3 after glycolation, indicating greater structural changes involving both donor and acceptor units. Therefore, the uniform and non-selective quenching of all peaks in gDPP-TTT suggests that the hole polaron is more delocalized throughout the entire conjugated backbone, including the DPP acceptor units.

To investigate the difference in the interactions of the ions and polymers, we performed MD simulations on neutral oligomeric models of the individual polymer chains in the same electrolyte environment with 0.2 M TBAPF₆ in acetonitrile solution. Details of the methodology including the parameters used for force-field validation can be found in the Section S3, Supporting Information. The spatial distribution of ions is illustrated in Figure 5 for cations (TBA⁺) and anions (PF₆[−]) showing the preferential accumulation around the acceptor and donor units, respectively. The ion distribution as a function of radius from the donor (TTVTT or TTT) and acceptor (DPP) atoms shows a greater density of ions nearer to the conjugated backbone for the glycolated copolymers. The amphipathic sidechains increase ion density by providing a polar environment and enhancing ion transport pathways to the bulk polymer, via electrolyte ions to OEG interactions.^[53] Whereas the branched alkyl sidechains provide no polar environment for ions and sterically hinder ions from diffusing toward the backbone. Consequently, the glycolated polymers show higher ion density near the backbone (below radius 0.7 nm).

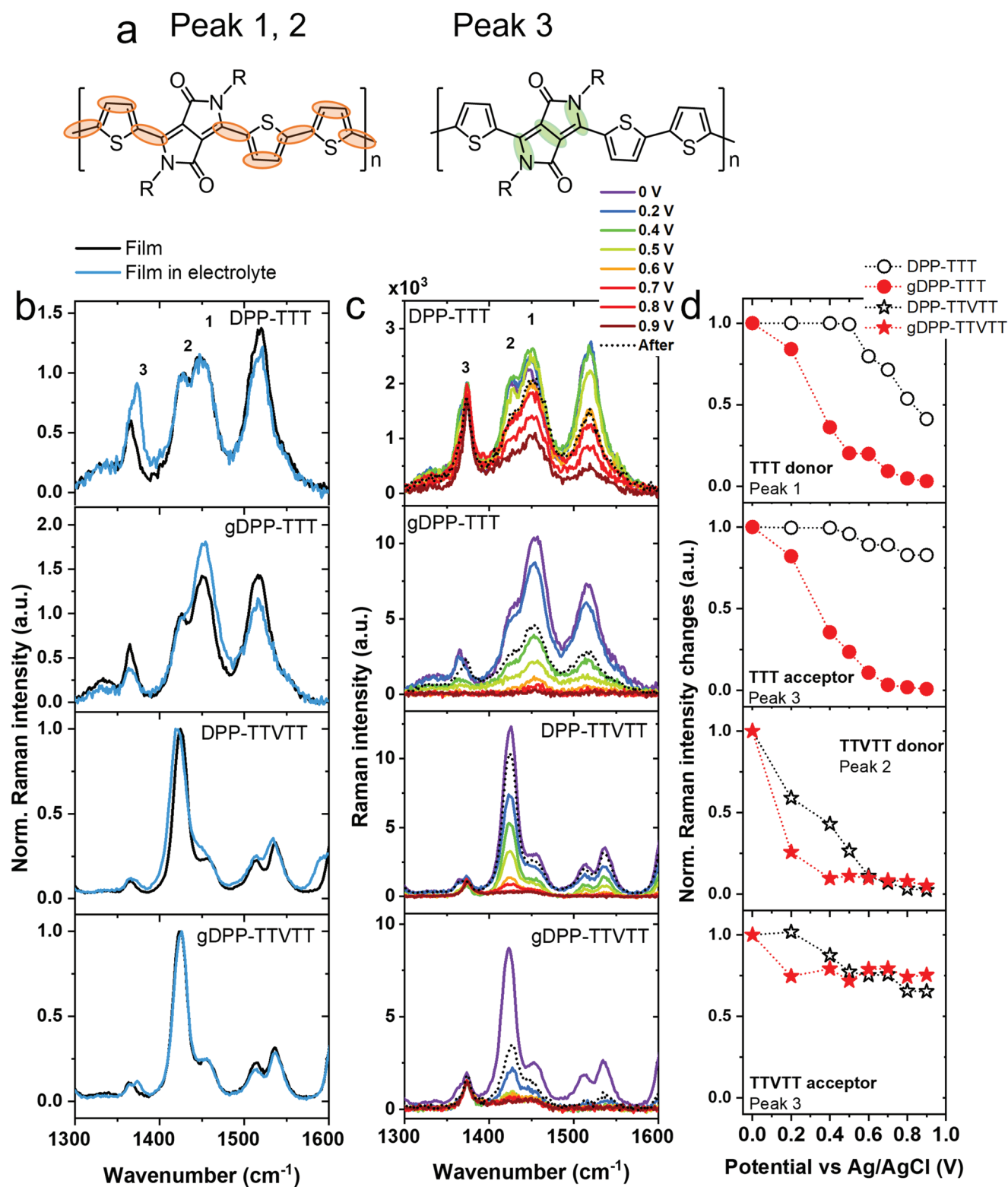


Figure 4. a) Raman peak assignments of the main 3 vibrational mode labelled on the spectra, which correspond to mainly donor (peaks 1 and 2) and acceptor units (peak 3). b) Raman spectra of the four copolymers thin films in air and immersed in acetonitrile electrolyte with TBAPF₆, using 488 nm excitation wavelength. c) In situ electrochemical Raman measurements using 488 nm excitation wavelength during chronoamperometric applied potentials at constant 0–0.9 V oxidizing bias. d) Normalized Raman intensity changes for peaks 1–3 extracted from the in situ electrochemical Raman spectra.

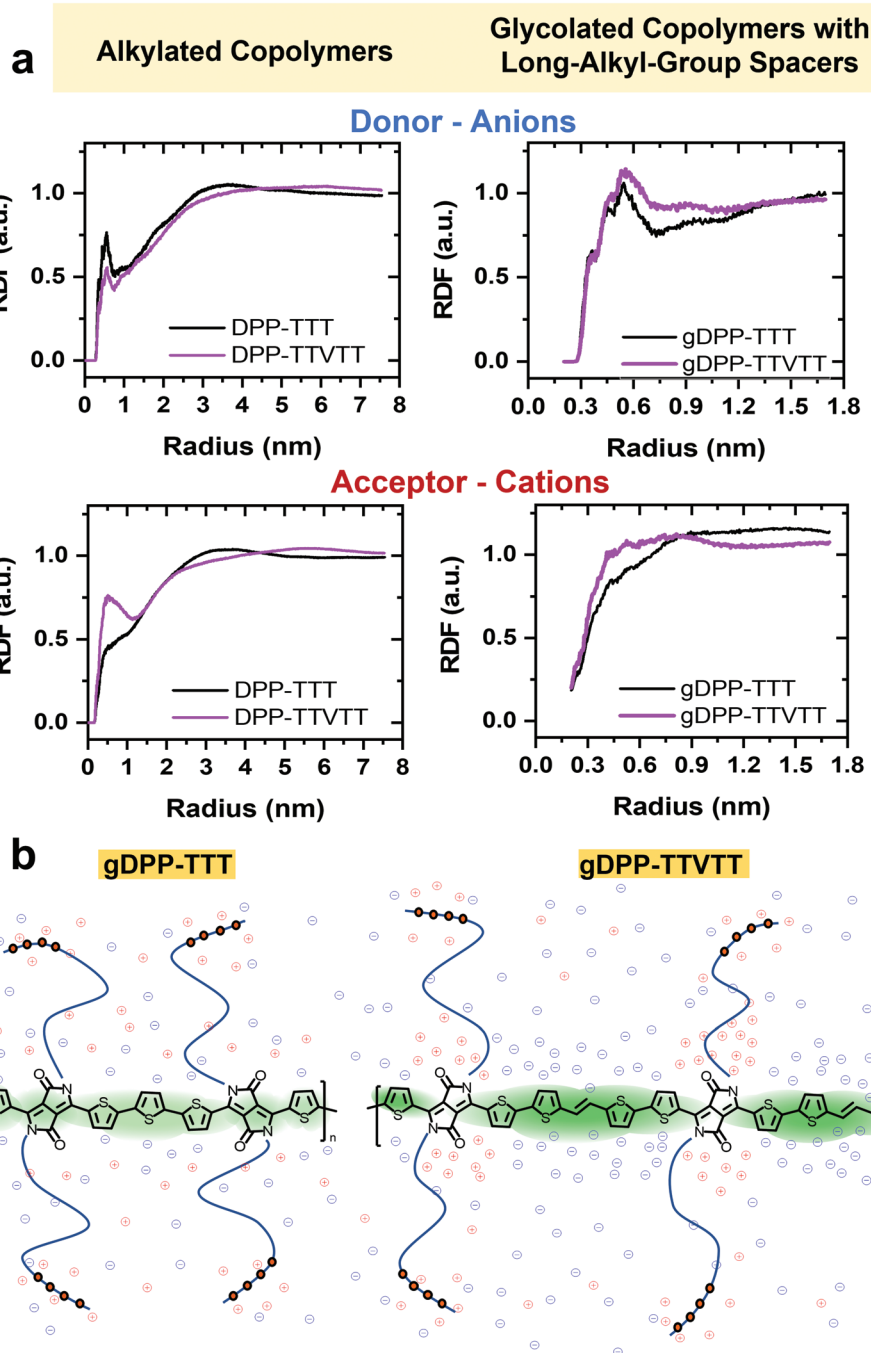


Figure 5. a) Graphs showing the radial distribution functions (RDF) of cations and anions from the conjugated backbone, calculated from MD simulations in acetonitrile with TBAPF₆. The donor-anion and acceptor-cation RDFs are significantly higher at lower radius for glycolated copolymers (below 0.7 nm), indicating more ions localized closer to the backbone compared to the alkylated counterparts. b) A schematic representation of the cation (red) and anion (blue) distribution in the glycolated copolymers. This illustrates the density of ions, which is greater in gDPP-TTVTT than DPP-TTT due to the reduced sidechain attachment frequency. Therefore, gDPP-TTVTT could result in more readily formed polarons (green) localized to the donor units, where there are more mobile anions.

Elongating the conjugated backbone with TTVTT also increases the RDF of ions around the backbone. One explanation for the difference in the spatial distribution of ions is the sidechain attachment frequency that is dependent on the conjugated backbone. There are more donor units in gDPP-TTVTT than gDPP-TTT, which increases the spacing between DPP

acceptor units. This lowers the effective sidechain attachment frequency along the polymer and enables greater ion density near the backbone. Specifically, there is greater cation density localized around the DPP acceptor units for gDPP-TTVTT compared to gDPP-TTT. This could result in a shielding effect in gDPP-TTVTT, thus preventing strong interactions between

anions and DPP acceptor. Indeed, the RDF show that gDPP-TTVTT has more anions close to the donor than acceptor units, compared to gDPP-TTT. Upon bias, the cation shielding anion interactions with the acceptor for gDPP-TTVTT could result in fewer structural changes of the DPP vibrational modes observed in the in situ Raman spectra. Moreover, Liu et al. has shown that the EG groups on amphipathic sidechains interact more strongly with cations compared to anions, meaning the use of a C₆ spacer has the effect of moving cation density away from the backbone.^[24] Similarly, the long-alkyl-group spacers used here could position the cations further away from the donor groups, to which the sidechains are attached. RDF comparisons between the alkyl sidechains and the OEG segments of the amphipathic sidechains are shown in Figure S16, Supporting Information, which suggest this is the case as there is higher cation density around the glycol portion of the amphiphilic side chain, compared to the alkyl side chain. As the amphipathic sidechains are positioned on the DPP units, the preferential cation-OEG interaction could ultimately allow more selective anion accumulation towards the donor moieties. A higher anion density initially around the TTVTT donor units could result in more readily stabilized polaron formation upon an oxidizing potential than without any mobile ion environment. This is clearly observed in the OECT V_{Th} and in situ spectroelectrochemistry, where gDPP-TTVTT forms polarons at lower applied potentials and quenches the ground state absorption band to a greater degree than gDPP-TTT. The HOMO energy level is likely a small factor in such differences as the energetics of the glycolated polymers are very similar, with gDPP-TTVTT being only shallower by 0.003 eV than gDPP-TTT. Giovannitti et al. previously showed that BDT accumulation-mode copolymers are stabilized by a strong electron-donating comonomer (MeOT2) that localizes charge density away from the BDT unit.^[27] This resulted in stable I_D under operation with pulsed V_G over a prolonged period. Similarly, the combination of the elongated conjugated backbone and long-alkyl-group spacer shifts polaron formation away from the DPP acceptor. As shown previously, gDPP-TTVTT has superior operational stability with no degradation of ON current during cycling of pulsed gating. Based on the MD, structural and OECT properties, gDPP-TTVTT can enable more ion accumulation and facilitate facile polaron formation localized to the donor to achieve greater OECT operational stability.

3. Conclusion

We have synthesized and investigated four DPP-based copolymers with TTT and TTVTT comonomers, branched alkyl and amphipathic sidechains, focusing on the structure–property relationships for OECT applications. Elongating the donor unit from TTT to TTVTT results in a highly ordered and “edge-on” molecular orientation, thus achieving the highest charge-transport properties as reflected in the OFET mobilities. Importantly, the long-alkyl-group spacers (C₁₂) in amphipathic sidechains prevents disruptions to the D–A polymer properties that provide efficient electronic charge transport. In fact, the amphipathic sidechains improve the in-plane π stacking by changing “face-on” to “edge-on” dominant orientation in gDPP-

TTT and in the case of gDPP-TTVTT, the high molecular “edge-on” packing is conserved. As a result, gDPP-TTVTT achieves the highest OECT transconductance and effective capacitance (61.9 S cm⁻¹, 1 mF cm⁻²) compared to gDPP-TTT (0.87 S cm⁻¹, 0.64 mF cm⁻²). The in situ structural analysis reveals that gDPP-TTVTT has faster and easier polaron formation with less structural changes in the DPP acceptor units. Accordingly, the MD shows gDPP-TTVTT with greater ion density around the backbone and anion accumulation near to the donor units. Such ion spatial distribution facilitates efficient polaron formation localized to the donor units, contributing towards gDPP-TTVTT's high OECT performance and operational stability. We achieve a fine balance of electronic and ion charge-transport properties by combining the use of an elongated conjugated backbone in D–A polymers and amphipathic sidechains with C₁₂ spacers. Our findings provide guidance for using long-alkyl-group spacers with D–A polymers, to improve optoelectronic and morphological properties that control charge transport and polaron formation for higher performing and stable OECTs.

4. Experimental Section

Device Fabrication and Characterization: Two configurations of OECT devices were fabricated using the sacrificial parylene peel-off method^[54] and photolithography^[55] with spin-coated DPP copolymer solutions and films were annealed at 180 °C for 20 min in air. The parylene peel-off OECTs used glass substrates while the photolithography method used a poly(ethylene terephthalate) (PET) substrate. The electrolytes were 0.1 M TBA PF₆ in acetonitrile solution and Ringer's solution from Sigma Aldrich. The output and transfer characteristics were measured using the Keysight B2902A precision source/measure unit for channel dimensions (W/L) of 100/10 μ m (acetonitrile electrolyte) and 2 mm/200 μ m (aqueous electrolyte) with active channel thicknesses of 40–50 nm. For acetonitrile devices with planar polymer-coated gold gate electrodes, output and transfer sweeps of $V_D = 0$ to -0.6 V and $V_G = 0$ to -0.8 V were measured at 0.1 V intervals. For aqueous devices with Ag pellet gate electrodes, output and transfer sweeps of $V_D = 0$ to -0.6 V and $V_G = 0$ to -0.6 V were measured at 0.1 V intervals.

OFET devices were made using prefabricated Fraunhofer silicon wafer substrates, consisting of a n-doped silicon wafer gate electrode, a silicon dioxide dielectric layer (230 nm), and source and drain electrodes formed of an ITO adhesion layer (10 nm) and gold (30 nm). The substrates were cleaned and deposited with DPP copolymer solution (5mg mL⁻¹ in CHCl₃) by spincoating at 2000 rpm for 30 s, then annealed at 180 °C for 20 min on a hot plate in air. The output and transfer characteristics were measured in a nitrogen filled glovebox using a Cascade Microtech Probe Station and a Keysight B2900A precision source measurement unit for channel lengths 5 μ m with a channel width of 2 mm. The transfer characteristics were measured at $V_D = -10$ and -60 V for a VG sweep of 20 to -60 V. The output characteristics were measured at 10 V intervals for $V_G = 0$ to -60 V and the V_D was swept from 20 to -60 V.

Electrochemistry: Chronoamperometry measurements used an electrochemical cell consisting of an acetonitrile electrolyte (0.1 M TBAPF₆), Pt counter electrode, Ag/AgCl reference electrode and fluorine doped tin oxide (FTO) glass coated in DPP copolymer as the working electrode. Using the Autolab potentiostat PGSTAT101, an oxidizing square-wave potential range between 0 and 1.0 V was applied for all biased in situ measurements. During a measurement, there were three stages of applied bias to the working electrode with respect to the Ag/AgCl reference: 0 V for 20 s, oxidizing potential of 90 s and 0 V for 20 s.

Cyclic voltammetry measurements also used Autolab potentiostat PGSTAT101 with the same sample preparation as above. The oxidizing potential was applied to the working electrode sweeping forward and backward between -0.1 and 1.2 V with a scan rate of 20 mV s⁻¹.

Electrochemical Impedance Spectroscopy: For the EIS measurements, copolymers were deposited by spin-coating (using the aforementioned deposition parameters) on microfabricated Au-patterned electrodes. EIS measurements were carried out using a 3-electrode configuration. Gold coated electrodes with the copolymers deposited on top were used as the working electrode, Pt mesh was used as a counter and Ag/AgCl as reference electrode. The electrolyte used was 0.1 M TBA PF₆ in acetonitrile solution. A plastic well was used to confine the electrolyte on top of the electrodes. EIS measurements were performed in the frequency range of 10⁵ to 0.1 Hz with a DC offset of 0, 0.5, and 0.8 V. The fitting analysis was performed using EC-Lab software. The effective capacitance was calculated using the following formula

$$C_{\text{eff}} = \frac{1}{2\pi fZ''} \quad (1)$$

UV-Vis Spectroscopy: The spectrophotometer model was Shimadzu UV-2600 and the FTO substrate's background contribution was subtracted from the transmittance using: Absorbance = log(%T_{substrate}/%T_{sample}). All spectroelectrochemistry experiments used chronoamperometry with the electrochemical cell.

Raman Spectroscopy: All Raman measurements used Renishaw inVia microscope in a back-scattering configuration using an argon ion laser at 488 and diode laser 785 nm, with 50% power of 9 and 130 mW, respectively. The in situ electrochemical Raman measurements were taken using the electrochemical cell positioned under the laser during constant applied oxidation potentials between 0 and 0.9 V. Before and after every measurement, 0 V potential was applied for 20 s.

Morphology: Grazing-incidence wide-angle X-ray scattering (GIWAXS) measurements were performed in the 3C-SAXSI beamline at the Pohang Accelerator Laboratory (PAL) using a monochromatized X-ray radiation source of 10.55 eV ($\lambda = 0.117$ nm) and a 2D charge-coupled device (CCD) detector (Mar165 CCD). The samples were mounted on a z-axis goniometer equipped with a vacuum chamber ($\approx 10^{-3}$ Torr), and the samples were fixed 0.201 m away from the CCD detector. The incident angle of each X-ray beam was 0.1°, and the scattering angles were determined from the positions of the reflected X-ray beam relative to the silicon substrate using precalibrated silver behenate.

Molecular Dynamics: Simulations were performed using GROMACS 2018.2.^[56,57] Electrostatics and Van-der-Waals forces were computed using the scalable particle mesh Ewald summation.^[58] Hydrogen bonds were constrained using a LINCS algorithm, allowing for 2 fs time steps. Initial configurations were prepared using GROMACS 2018.2 and Packmol.^[59] Trajectories were analyzed using PyMOL.^[60] Initially energy minimization was performed on all simulations using the steep integration method, and a time step of 1 fs, until the change in energy was less than numerical accuracy. After energy minimization, candidate crystals were simulated in NVT at 300 K for 500 000 steps at 2 fs per step. Temperature coupling was achieved through the velocity-rescale algorithm.^[61] Following this, a 50 ns NPT production run was performed at 300 K and 1 bar using Berendsen temperature and pressure coupling.^[62] Intermolecular forces were calculated with Particle-Mesh-Ewald summations, with a 1 nm cut-off distance.

Forcefield parameters were broadly based, and validated by, the methodology outlined in a previous study.

Supporting Information

Supporting Information is available from the Wiley Online Library or from the author.

Acknowledgements

The authors acknowledge the UK EPSRC for the Plastic Electronics Centre for Doctoral Training (EP/L016702/1) funding. The research

was also supported by the UK Department for Business, Energy and Industrial Strategy (BEIS) through the National Measurement System. This work was supported by NRF (2021R1A2B5B03086367) and NRF (2018R1C1B6006177). N.S. and J.N. acknowledge funding from the European Research Council under the European Union's Horizon 2020 research and innovation program (grant agreement no 742708, project CAPaCITY).

Conflict of Interest

The authors declare no conflict of interest.

Data Availability Statement

Full force field parameter files and topology files used in this work are available in GitHub at <https://github.com/nicholas9182/0011>. Other data that support the findings of this study are available from the corresponding author upon reasonable request.

Keywords

accumulation mode, amphipathic sidechains, conjugated polymers, long-alkyl-group spacers, organic electrochemical transistors

Received: March 20, 2022

Revised: April 8, 2022

Published online:

- [1] F. Decataldo, V. Druet, A.-M. Pappa, E. Tan, A. Savva, C. Pitsalidis, S. Inal, J.-S. Kim, B. Fraboni, R. M. Owens, D. Iandolo, *Flex. Print. Electron.* **2019**, *4*, 044006.
- [2] N. Coppedè, M. Giannetto, M. Villani, V. Lucchini, E. Battista, M. Careri, A. Zappettini, *Org. Electron.* **2020**, *78*, 105579.
- [3] A. M. Pappa, D. Ohayon, A. Giovannitti, I. P. Maria, A. Savva, I. Uguz, J. Rivnay, I. McCulloch, R. M. Owens, S. Inal, *Sci. Adv.* **2018**, *4*, eaat0911.
- [4] J. Nightingale, C. Pitsalidis, A.-M. Pappa, E. Tan, K. Stewart, R. M. Owens, J.-S. Kim, *J. Mater. Chem. C* **2020**, *8*, 8846.
- [5] D. Moia, A. Giovannitti, A. A. Szumska, I. P. Maria, E. Rezasoltani, M. Sachs, M. Schnurr, P. R. F. Barnes, I. McCulloch, J. Nelson, *Energy Environ. Sci.* **2019**, *12*, 1349.
- [6] C. Pitsalidis, A.-M. Pappa, M. Porel, C. M. Artim, G. C. Faria, D. D. Duong, C. A. Alabi, S. Daniel, A. Salleo, R. M. Owens, C. Pitsalidis, A. Pappa, R. M. Owens, M. Porel, C. M. Artim, C. A. Alabi, S. Daniel, G. C. Faria, D. D. Duong, A. Salleo, *Adv. Mater.* **2018**, *30*, 1803130.
- [7] C. Pitsalidis, M. P. Ferro, D. Iandolo, L. Tzounis, S. Inal, R. M. Owens, *Sci. Adv.* **2018**, *4*, eaat4253.
- [8] D. Khodagholy, J. Rivnay, M. Sessolo, M. Gurfinkel, P. Leleux, L. H. Jimison, E. Stavrinidou, T. Herve, S. Sanaur, R. M. Owens, G. G. Malliaras, *Nat. Commun.* **2013**, *4*, 2133.
- [9] C. M. Proctor, J. Rivnay, G. G. Malliaras, *J. Polym. Sci. Part B: Polym. Phys.* **2016**, *54*, 1433.
- [10] J. Rivnay, P. Leleux, M. Sessolo, D. Khodagholy, T. Hervé, M. Flocchi, G. G. Malliaras, *Adv. Mater.* **2013**, *25*, 7010.
- [11] J. Rivnay, P. Leleux, M. Ferro, M. Sessolo, A. Williamson, D. a. Koutsouras, D. Khodagholy, M. Ramuz, X. Strakosas, R. M. Owens, C. Benar, J.-M. Badier, C. Bernard, G. G. Malliaras, *Sci. Adv.* **2015**, *1*, e1400251.

- [12] S. Inal, J. Rivnay, P. Leleux, M. Ferro, M. Ramuz, J. C. Brendel, M. M. Schmidt, M. Thelakkat, G. G. Malliaras, *Adv. Mater.* **2014**, *26*, 7450.
- [13] E. Zeglio, M. Vagin, C. Musumeci, F. N. Ajjan, R. Gabrielsson, X. T. Trinh, N. T. Son, A. Maziz, N. Solin, O. Inganäs, *Chem. Mater.* **2015**, *27*, 6385.
- [14] M. Y. Teo, N. Kim, S. Kee, B. S. Kim, G. Kim, S. Hong, S. Jung, K. Lee, *ACS Appl. Mater. Interfaces* **2017**, *9*, 819.
- [15] C. B. Nielsen, A. Giovannitti, D. Sbircea, E. Bandiello, M. R. Niazi, D. A. Hanifi, M. Sessolo, A. Amassian, G. G. Malliaras, J. Rivnay, I. McCulloch, *J. Am. Chem. Soc.* **2016**, *138*, 10252.
- [16] A. Giovannitti, C. B. Nielsen, D.-T. Sbircea, S. Inal, M. Donahue, M. R. Niazi, D. A. Hanifi, A. Amassian, G. G. Malliaras, J. Rivnay, I. McCulloch, *Nat. Commun.* **2016**, *7*, 13066.
- [17] A. A. Szumska, I. P. Maria, L. Q. Flagg, A. Savva, J. Surgailis, B. D. Paulsen, D. Moia, X. Chen, S. Griggs, J. T. Mefford, R. B. Rashid, A. Marks, S. Inal, D. S. Ginger, A. Giovannitti, J. Nelson, *J. Am. Chem. Soc.* **2021**, *143*, 14795.
- [18] P. Schmode, D. Ohayon, P. M. Reichstein, A. Savva, S. Inal, M. Thelakkat, *Chem. Mater.* **2019**, *31*, 5286.
- [19] A. Giovannitti, D.-T. Sbircea, S. Inal, C. B. Nielsen, E. Bandiello, D. A. Hanifi, M. Sessolo, G. G. Malliaras, I. McCulloch, J. Rivnay, *Proc. Natl. Acad. Sci. USA* **2016**, *113*, 12017.
- [20] A. Giovannitti, I. P. Maria, D. Hanifi, M. J. Donahue, D. Bryant, K. J. Barth, B. E. Makdah, A. Savva, D. Moia, M. Zetek, P. R. F. Barnes, O. G. Reid, S. Inal, G. Rumbles, G. G. Malliaras, J. Nelson, J. Rivnay, I. McCulloch, *Chem. Mater.* **2018**, *30*, 2945.
- [21] P. Schmode, A. Savva, R. Kahl, D. Ohayon, F. Meichsner, O. Dolynchuk, T. Thurn-Albrecht, S. Inal, M. Thelakkat, *ACS Appl. Mater. Interfaces* **2020**, *12*, 13029.
- [22] I. P. Maria, B. D. Paulsen, A. Savva, D. Ohayon, R. Wu, R. Hallani, A. Basu, W. Du, T. D. Anthopoulos, S. Inal, J. Rivnay, I. McCulloch, A. Giovannitti, *Adv. Funct. Mater.* **2021**, *31*, 2008718.
- [23] M. Moser, Y. Wang, T. C. Hidalgo, H. Liao, Y. Yu, J. Chen, J. Duan, F. Moruzzi, S. Griggs, A. Marks, N. Gasparini, A. Wadsworth, S. Inal, I. McCulloch, W. Yue, *Mater. Horiz.* **2022**, *9*, 973.
- [24] J. Liu, G. Ye, H. G. O. Potgieser, M. Koopmans, S. Sami, M. I. Nugraha, D. R. Villalva, H. Sun, J. Dong, X. Yang, X. Qiu, C. Yao, G. Portale, S. Fabiano, T. D. Anthopoulos, D. Baran, R. W. A. Havenith, R. C. Chiechi, L. J. A. Koster, *Adv. Mater.* **2021**, *33*, 2006694.
- [25] L. Q. Flagg, C. G. Bischak, J. W. Onorato, R. B. Rashid, C. K. Luscombe, D. S. Ginger, *J. Am. Chem. Soc.* **2019**, *141*, 4345.
- [26] H. Jia, Z. Huang, P. Li, S. Zhang, Y. Wang, J.-Y. Y. Wang, X. Gu, T. Lei, *J. Mater. Chem. C* **2021**, *9*, 4927.
- [27] A. Giovannitti, K. J. Thorley, C. B. Nielsen, J. Li, M. J. Donahue, G. G. Malliaras, J. Rivnay, I. McCulloch, *Adv. Funct. Mater.* **2018**, *28*, 1706325.
- [28] M. Moser, A. Savva, K. Thorley, B. D. Paulsen, T. C. Hidalgo, D. Ohayon, H. Chen, A. Giovannitti, A. Marks, N. Gasparini, A. Wadsworth, J. Rivnay, S. Inal, I. McCulloch, *Angew. Chem., Int. Ed.* **2021**, *60*, 7777.
- [29] K. Guo, J. Bai, Y. Jiang, Z. Wang, Y. Sui, Y. Deng, Y. Han, H. Tian, Y. Geng, *Adv. Funct. Mater.* **2018**, *28*, 1801097.
- [30] M. Hamsch, T. Erdmann, A. R. Chew, S. Bernstorff, A. Salleo, A. Kiriya, B. Voit, S. C. B. Mannsfeld, *J. Mater. Chem. C* **2019**, *7*, 3665.
- [31] H. Yu, K. H. Park, I. Song, M. J. Kim, Y. H. Kim, J. H. Oh, *J. Mater. Chem. C* **2015**, *3*, 11697.
- [32] S. H. Yu, K. H. Park, Y.-H. Kim, D. S. Chung, S.-K. Kwon, *Macromolecules* **2017**, *50*, 4227.
- [33] I. Kang, H.-J. Yun, D. S. Chung, S.-K. Kwon, Y.-H. Kim, *J. Am. Chem. Soc.* **2013**, *135*, 14896.
- [34] Y. Wang, A. Hamidi-Sakr, J. Surgailis, Y. Zhou, H. Liao, J. Chen, G. Zhu, Z. Li, S. Inal, W. Yue, *J. Mater. Chem. C* **2021**, *9*, 13338.
- [35] N. A. Kukhta, A. Marks, C. K. Luscombe, *Chem. Rev.* **2022**, *122*, 4325.
- [36] D. A. Bernards, G. G. Malliaras, *Adv. Funct. Mater.* **2007**, *17*, 3538.
- [37] S. E. Doris, A. Pierre, R. A. Street, *Adv. Mater.* **2018**, *30*, 1706757.
- [38] D. T. Duong, Y. Tuchman, P. Chakthranont, P. Cavassin, R. Colucci, T. F. Jaramillo, A. Salleo, G. C. Faria, *Adv. Electron. Mater.* **2018**, *4*, 1800090.
- [39] M. J. Panzer, C. R. Newman, C. D. Frisbie, *Appl. Phys. Lett.* **2005**, *86*, 103503.
- [40] H. F. Haneef, A. M. Zeidell, O. D. Jurchescu, *J. Mater. Chem. C* **2020**, *8*, 759.
- [41] W. Shi, Y. Zheng, J. Yu, A. D. Taylor, H. E. Katz, *Appl. Phys. Lett.* **2016**, *109*, 143301.
- [42] H. Klauk, *Chem. Soc. Rev.* **2010**, *39*, 2643.
- [43] Z. Wang, Z. Liu, L. Ning, M. Xiao, Y. Yi, Z. Cai, A. Sadhanala, G. Zhang, W. Chen, H. Sirringhaus, D. Zhang, *Chem. Mater.* **2018**, *30*, 3090.
- [44] B. Meng, H. Song, X. Chen, Z. Xie, J. Liu, L. Wang, *Macromolecules* **2015**, *48*, 4357.
- [45] M. Moser, L. R. Savagian, A. Savva, M. Matta, J. F. Ponder, T. C. Hidalgo, D. Ohayon, R. Hallani, M. Rejsjalali, A. Troisi, A. Wadsworth, J. R. Reynolds, S. Inal, I. McCulloch, *Chem. Mater.* **2020**, *32*, 6618.
- [46] S. Wood, J. Wade, M. Shahid, E. Collado-Fregoso, D. D. C. Bradley, J. R. Durrant, M. Heeney, J.-S. Kim, *Energy Environ. Sci.* **2015**, *8*, 3222.
- [47] F. C. Spano, C. Silva, *Annu. Rev. Phys. Chem.* **2014**, *65*, 477.
- [48] E. Tan, A. Pappa, C. Pitsalidis, J. Nightingale, S. Wood, F. A. Castro, R. M. Owens, J. Kim, *Biotechnol. Bioeng.* **2020**, *117*, 291.
- [49] S. Limbu, S. Pont, A. B. Doust, S. Kwon, P. Fuller, E. Tan, J. R. Durrant, J.-S. Kim, *Adv. Mater. Interfaces* **2019**, *6*, 1801763.
- [50] J. Luke, E. M. Speller, A. Wadsworth, M. F. Wyatt, S. Dimitrov, H. K. H. Lee, Z. Li, W. C. Tsoi, I. McCulloch, D. Bagnis, J. R. Durrant, J.-S. Kim, *Adv. Energy Mater.* **2019**, *9*, 1803755.
- [51] W. C. Tsoi, D. T. James, J. S. Kim, P. G. Nicholson, C. E. Murphy, D. D. C. Bradley, J. Nelson, J.-S. Kim, *J. Am. Chem. Soc.* **2011**, *133*, 9834.
- [52] K. Stewart, S. Limbu, J. Nightingale, K. Pagano, B. Park, S. Hong, K. Lee, S. Kwon, J.-S. Kim, *J. Mater. Chem. C* **2020**, *8*, 15268.
- [53] Z. Xue, D. He, X. Xie, *J. Mater. Chem. A* **2015**, *3*, 19218.
- [54] E. Stavrinidou, P. Leleux, H. Rajaona, D. Khodagholy, J. Rivnay, M. Lindau, S. Sanaur, G. G. Malliaras, *Adv. Mater.* **2013**, *25*, 4488.
- [55] J. E. Tyrrell, M. G. Boutelle, A. J. Campbell, *Adv. Funct. Mater.* **2021**, *31*, 2007086.
- [56] S. Pronk, S. Páll, R. Schulz, P. Larsson, P. Bjelkmar, R. Apostolov, M. R. Shirts, J. C. Smith, P. M. Kasson, D. Van Der Spoel, B. Hess, E. Lindahl, *Bioinformatics* **2013**, *29*, 845.
- [57] D. Van Der Spoel, E. Lindahl, B. Hess, G. Groenhof, A. E. Mark, H. J. C. Berendsen, *J. Comput. Chem.* **2005**, *26*, 1701.
- [58] B. Hess, C. Kutzner, D. Van Der Spoel, E. Lindahl, *J. Chem. Theory Comput.* **2008**, *4*, 435.
- [59] L. Martínez, R. Andrade, E. G. Birgin, J. M. Martínez, *J. Comput. Chem.* **2009**, *30*, 2157.
- [60] Schrodinger, LLC. The PyMOL molecular graphics system, version 1.8, 2015.
- [61] G. Bussi, D. Donadio, M. Parrinello, *J. Chem. Phys.* **2007**, *126*, 014101.
- [62] H. J. C. Berendsen, D. van der Spoel, R. van Drunen, *Comput. Phys. Commun.* **1995**, *91*, 43.